sensors

MDPI

Article

Electric Susceptibility at Partial Coverage of a Circular One-Side Access Capacitive Sensor with Rigid Polyurethane Foams

Ilze Beverte

Institute for Mechanics of Materials, University of Latvia, LV-1004 Riga, Latvia; ilze.beverte@lu.lv; Tel.: +371-29-46-42-50

Abstract: The capability of dielectric measurements was significantly increased with the development of capacitive one-side access physical sensors. Complete samples give no opportunity to study electric susceptibility at a partial coverage of the one-side access sensor's active area; therefore, partial samples are proposed. The electric susceptibility at the partial coverage of a circular one-side access sensor with cylinders and shells is investigated for polyurethane materials. The implementation of the relative partial susceptibility permitted us to transform the calculated susceptibility data to a common scale of 0.0–1.0 and to outline the main trends for PU materials. The partial susceptibility, relative partial susceptibility, and change rate of relative partial susceptibility exhibited dependence on the coverage coefficient of the sensor's active area. The overall character of the curves for the change rate of the relative partial susceptibility, characterised by slopes of lines and the ratio of the change rate in the centre and near the gap, corresponds with the character of the surface charge density distribution curves, calculated from mathematical models. The elaborated methods may be useful in the design and optimization of capacitive OSA sensors of other configurations of electrodes, independent of the particular technical solution.

Keywords: capacitive sensor; one-side access; circular symmetry; polyurethane foams; partial coverage; permittivity; electric susceptibility; surface charge

check for updates

Citation: Beverte, I. Electric Susceptibility at Partial Coverage of a Circular One-Side Access Capacitive Sensor with Rigid Polyurethane Foams. *Sensors* **2024**, *24*, 3003. https://doi.org/10.3390/s24103003

Academic Editor: Jeong In Han

Received: 18 March 2024
Revised: 22 April 2024
Accepted: 6 May 2024
Published: 9 May 2024

Copyright: © 2024 by the author. Licensee MDPI, Basel, Switzerland. This article is an open access article distributed under the terms and conditions of the Creative Commons Attribution (CC BY) license (https://creativecommons.org/licenses/by/4.0/).

1. Introduction

In the non-destructive evaluation of dielectric materials, in the frequency band up to 10 MHz, the capacitance method is one of the main testing methods [1]. The capability of dielectric measurements was significantly increased with the development of capacitive one-side access (OSA) physical sensors, which permitted non-destructive testing and the characterization of materials without preparation of specimens [2–5], by merely pushing the sensor against one side of the test object. Several problems exist when working with capacitive OSA sensors: they excite test objects with a non-homogeneous electric field, have low sensing (geometric) capacitances, and high stray capacitances; bulk reference specimens are needed, whose minimum thickness (height) is limited by the effective depth of the penetration of the electrical field. Contrary to the parallel-plate capacitive sensors, working with a homogeneous electric field, there are no simple formulas for calculating the sensing capacities of OSA sensors at a complete or partial coverage with a dielectric [3,6,7].

The intensity maximum of a low-frequency excitation field is situated in the direct vicinity of the active area of a capacitive OSA transducer's electrodes [2]. The penetration depth of the excitation field into the test object determines the lateral dimensions (height/thickness) appropriate for permittivity measurements [2,3,7,8]. In [7], the penetration depth of a concentric, coplanar, and capacitive OSA sensor was estimated by identifying the test object's height, for which the capacitance is 3% or 10% smaller than its value when in contact with a similar, but infinitely high, test-piece. For a given sensor configuration, the sensor penetration depth increases as the test object's permittivity increases. The measured permittivity of polyurethane foams and PTFE was investigated in [8] with a

dependence on the OSA sensor's working volume, when the latter is filled partly along the lateral dimension (height) of the samples. The height of the samples was gradually decreased, and a 3% criterion to detect the penetration depth was applied.

Mathematical modelling and numerical calculations in [7] outlined an optimal two-electrode OSA sensor configuration for a given width of the gap, which ensured the maximum transcapacitance. Utilizing the spatial domain Green's functions and the method of moments [9,10], the sensor surface charge density was calculated, and then the sensor's transcapacitance was determined from its surface charge. In [11], the charge density on circular electrodes of a two-electrode OSA sensor was assumed to be constant, and the average potential of the electrodes was calculated. In [12,13], a circular three-electrode OSA sensor is considered. A jump in the normal component of the electric field across an interface is defined, which would be equal to the surface charge density in the absence of ohmic conduction in the medium. The jump is zero at every interface except in the plane of the electrodes. For every Fourier–Bessel mode [14], the jump is related to the difference in the surface capacitance density.

The regions of an OSA sensor that contribute most to the sensor's capacitance are the outer edge of the inner electrode and the inner edge of the outer electrode, where the surface charge density is the highest [6,7,15]. This results in a low capacitance of the sensor. The most sensitive zone of the sensor closely corresponds to the location of the gap between its two electrodes, and for sensors with a relatively large radius of the inner electrode, there will be an insensitive zone at the centre [6]. Empirical knowledge of a certain physical property of dielectric material, dependent on the surface charge distribution on the active area, would facilitate a performance evaluation, modelling, and the design of optimal proportions of electrodes' dimensions [16–22].

PU foam is a "Polymer-gas" composite, which has the same matrix—monolithic polyurethane, in the whole range of densities, i.e., 30–1280 kg/m^3 [23–25]. For light-weight PU foams (density of 30 kg/m^3), permittivity $\varepsilon \approx 1.065$, for medium weight (550 kg/m^3), $\varepsilon \approx 2.10$, and for monolithic polyurethane (1280 kg/m^3), $\varepsilon \approx 3.35$ (all at a frequency of 1 kHz) [8,26,27]. Rigid polyurethane (PU) foams [23,24] exhibit low dielectric interference and nearly non-dispersive permittivity; therefore, excellent dielectric performance can be ensured in a wide frequency range. The foams are comparatively easy to process mechanically, which makes them appropriate for a study of permittivity and electric susceptibility at a partial coverage of an OSA sensor.

A complete dielectric sample covers the total active area of the OSA sensor, and the permittivity, measured for it, is the true permittivity, which characterises the overall effect of the electric charge on the sample. Complete samples provide no opportunity to study permittivity and electric susceptibility at a partial coverage of the active area and to estimate their correspondence to the charge density distribution. Therefore, partial samples are proposed for measurements of permittivity and the study of electric susceptibility. This study aims to investigate electric susceptibility at a partial coverage of a circular capacitive OSA physical sensor with samples—cylinders and shells, made from PU foams and monolithic polyurethanes. A transition to the relative partial electric susceptibility permitted us to transform the calculated data of the partial susceptibility to a common scale of 0.0–1.0 and to outline the main trends for PU materials of significantly differing true permittivity. The change rate of the relative partial susceptibility with a dependence on the coverage coefficients of the active area and the subsample's radius is evaluated. A comparison with the results of other authors is made.

2. Materials and Methods

2.1. Polyurethane Materials

Rigid closed-cell petrochemical PU foams were made at apparent core densities of 30 kg/m^3 < ρ < 80 kg/m^3, in blocks, according to the formulation in [8,26,27]. The apparent core density (density) was determined in correspondence with ISO 845:2006 [28]. The difference in densities was achieved by varying the amount of physical or chemical blowing

agents. To make monolithic polyurethane, a liquid mixture of the same formulation as for PU foams was poured into polyethylene ampoules with an inner diameter of 25.4 mm and a length of 115 mm; no foaming agent was added. The ampoules were centrifuged for ~20 min at 5000 rpm in a centrifuge Sigma 3-30KS (Sigma Laborzentrifugen GmbH, Osterode am Harz, Germany) [26]. The technology ensured that ≈2/3 of the length of the cylindrical part of the PU rods was free from gaseous inclusions.

Industrially manufactured rigid petrochemical PU foam SikaBlock, with densities of 85 kg/m^3 ≤ ρ ≤ 415 kg/m^3, monolithic polyurethane SikaBlock-M945, and a comparative material—monolithic epoxy LAB 975 NEW—were acquired from Sika JSC (Baar, Switzerland).

Depending on the production technology, PU foams can exhibit anisotropy of structure and properties [29,30], when the permittivity and electric susceptibility ε_{ij} and χ_{ij} are the 2nd-rank tensors. Only isotropic PU foams are considered further.

2.2. Capacitive One-Side Access Sensor

Permittivity was measured with an experimental dielectric spectrometer equipped with a capacitive sensor of the one-side access (OSA) type [3,8,26,27]. The dielectric sample was placed on the active area of the sensor, Figure 1, and excited via electrodes, by an electrical field generated by sinusoidal voltage signals. The amplitude value of the sinusoidal excitation signals was U_0 = 20 V. The signals were generated at discrete frequencies, increasing in a geometric progression as follows:

$$\begin{gathered} f_n = f_1, 2f_1, \ldots, 2^{(n-1)}f_1 \text{ Hz, where } f_1 = 10 \text{ Hz, } n = 1, 2, \ldots, 16, \\ f = 10, 20, \ldots, 327{,}680 \text{ Hz,} \end{gathered} \quad (1)$$

where n is the ordeal number of a frequency. In the capacitive sensor system (CSS), the driven electrode №1 and sensing electrode №2 are connected to the multi-frequency excitation generator; the driven electrode is connected directly to the sensing electrode through a reference capacitor C_{ref} [3].

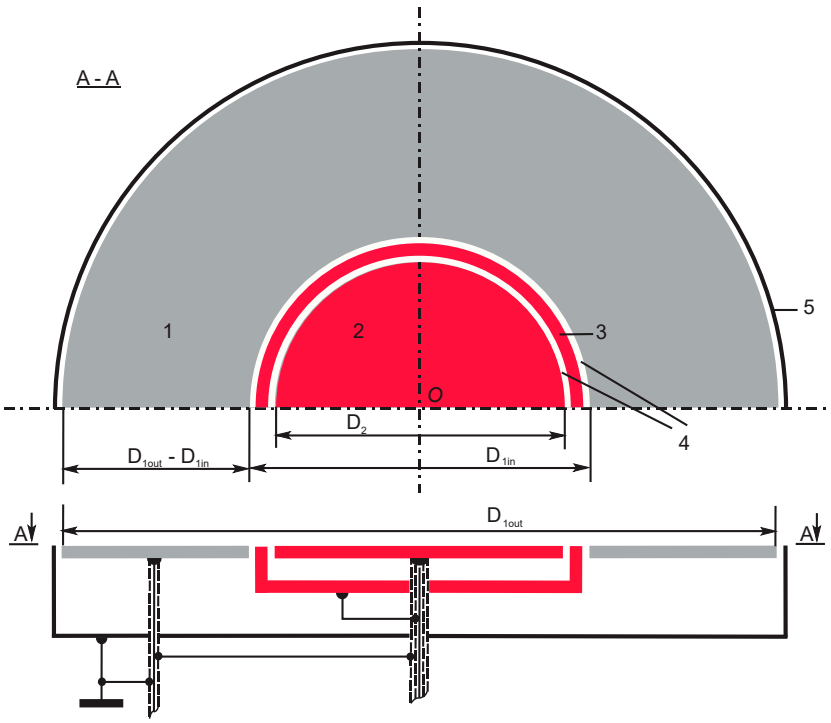


Figure 1. The electrodes: (1) Driven (D_{1in} = 21.0 mm, D_{1out} = 45.0 mm), (2) Sensing (diameter D_2 = 16.8 mm), and (3) Guard (width of 1.00 mm) as well as (4) Insulator (width of 0.55 mm) and (5) Grounded screen of the OSA sensor.

To carry out stray-immune capacitance measurements, the sensing electrode, the reference capacitor, and the unity gain buffer amplifier are covered with a screen, which forms the guard electrode №3 on the active area of CSS around the sensing electrode, as shown in Figure 1. The guard electrode is fed by the same voltage as the sensing electrode (active guarding) through a voltage follower, thus suppressing the electric field between the driven electrode and the sensing electrode outside the sensor's active surface.

The accuracy of the spectrometer in permittivity measurements, in conditions of repeatability, was estimated with the expanded uncertainty $U_S95.45\% = \pm 0.01$ [8,31,32]. The calibration of the spectrometer was made before each measurement, with respect to permittivity, delivered by the sensor in the air. Three consecutive measurements of permittivity spectra were made for each data point.

2.3. Dielectric Losses

The dielectric loss part $\varepsilon''(f)$ of the complex permittivity $\widetilde{\varepsilon}(jf) = \varepsilon'(f) - j\varepsilon''(f)$ was evaluated for PU foams and monolithic polyurethane, using data from direct measurements and scientific information sources [8]. The dielectric losses of PU materials were measured with a broadband dielectric spectrometer BDS-50 (Novocontrol Technologies GmbH & Co. KG, Montabaur, Germany), comprising a parallel plate capacitor, for samples with a diameter of 30 mm and a thickness of 2 mm. Five measurements were made for each data point. The real and the imaginary parts $\varepsilon'(f)$ and $\varepsilon''(f)$ were compared.

2.4. Lateral Dimensions of a Complete Sample

In order to study the special cases of the partial coverage of the OSA sensor's active area, several benchmark experiments were carried out (Points 2.4., 2.5., 2.6., and 2.8.), and their results were analysed (Points 4.2., 4.3., 4.4., and 4.6.).

Let us consider a PU foam sample with a diameter $d = D_0 = 45$ mm and thickness $t = 65$ mm. The cross-sectional surface of the sample covers the whole active area of the circular OSA sensor, and the thickness considerably exceeds the penetration depth of the low-frequency electric field into the PU foams [1 d c, PTFE]. The impact of the lateral dimension (the thickness) of such a sample on the permittivity was studied. The intensity maximum of the dielectric spectrometer's low-frequency excitation field is situated in the direct vicinity of the active area of the OSA sensor's electrodes [2,8]. Therefore, first, the permittivity of the samples was determined. Then, a thin layer, thickness $\Delta t = 0.5$–2.0 mm, was cut from the top of the sample, and the permittivity of the remaining part was measured. Then, the next layer with a thickness $\Delta t = 0.5$–2.0 mm was cut, etc. The experimental data were plotted against the thickness values of the sample. Then the penetration depth of the electric field of a certain frequency f was defined as such a thickness $t_{3\%}$ of a sample, at which the electric susceptibility is 3% less than the true susceptibility $\chi_t = \varepsilon_t - 1.0$ of an infinitely thick sample, $\chi = 97\%\ \chi_t$ [7,8].

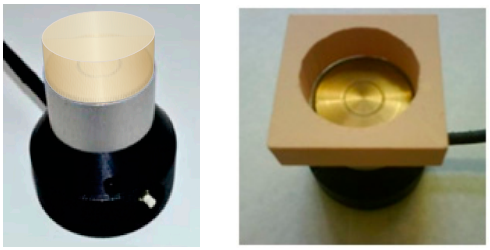
A sample is considered complete if (1) its cross-sectional surface covers the whole active area of the sensor and (2) its thickness equals or exceeds the penetration depth of the electric field of a certain frequency into the given dielectric. A measurement on a complete sample provides the true permittivity ε_t of the dielectric material.

The reading of the dielectric spectrometer for any sample, which either (1) covers the active area of the sensor partially and/or (2) has a thickness, smaller than the penetration depth of the electric field of a certain frequency, is denoted further as "The measured permittivity ε_m".

2.5. Transversal Dimensions of Samples

The impact of the transversal dimensions of a sample on the permittivity was studied for parallelepiped-shaped samples of dimensions (1) $20 \times 65 \times 65$ mm and (2) $20 \times 45 \times 45$ mm and for (3) cylindrical samples with a diameter $d = D_0 = 45$ mm and a thickness of 20 mm, Figure 2a. The "(2)" parallelepipeds were made from the "(1)" ones, and then the cylinders were made from the "(2)" parallelepipeds. All three kinds of samples are considered

complete, since covering the whole active area is ensured. The permittivity of samples "(1)", "(2)", and "(3)" was determined for lab-made PU foam (50 kg/m^3), PU foam SikaBlock-M150 (144 kg/m^3), and SikaBlock-M450 (415 kg/m^3).



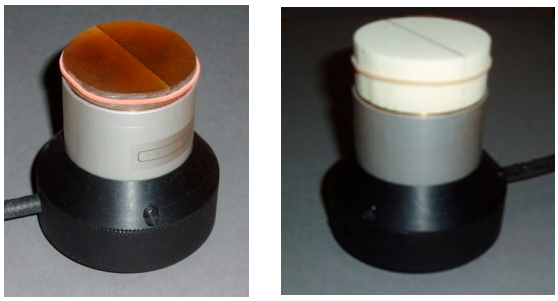
(**a**) (**b**)

Figure 2. PU foam samples on the active area of the sensor: (**a**) A cylindrical complete sample with a diameter d = D_0 = 45 mm and a thickness of 20 mm and (**b**) a parallelepiped with a concentric cylindrical hole.

Another experiment was performed for three other parallelepipeds of the kind "(1)" (20 × 65 × 65 mm), made from the same PU foams. First, the permittivity was measured for each parallelepiped, and then a concentric cylindrical hole, diameter d ≈ D_0 = 45 mm, was made in each sample. The sample was placed on the isolated circular case of the sensor, Figure 2b, and a reading of the spectrometer was made.

2.6. Inner Vertical Surfaces

The impact of inner vertical surfaces in a complete, circular cylindrical sample on the measured permittivity was estimated experimentally. The task arises due to the limited transversal and lateral dimensions of the lab-made monolithic PU rods, when only one semi-cylinder (D_0 = 45 mm and h = 12 mm) can be made from a PU rod. Side by side, the two semi-cylinders form a combined sample with two inner vertical surfaces along the diagonal. The semi-cylinders were pushed together, fixed firmly with an elastic band along the outer circular perimeter, Figure 3a, and the reading of the spectrometer was made.



(**a**) (**b**)

Figure 3. Complete samples with inner vertical surfaces on the active area of the sensor: (**a**) Lab-made monolithic PU and (**b**) PU foam SikaBlock-M450.

The experiment was carried out also for a monolithic PU SikaBlock-M960. The dielectric SikaBlock-M960 was available in blocks of sufficiently large dimensions to make complete cylindrical samples of thickness t = 12 mm and diameter D_0 = 45 mm. First, the permittivity of a complete, continuous sample was measured, and then it was cut into two semi-cylindrical parts. The parts were pushed together and fixed firmly with the elastic band, and the reading of the spectrometer was made. The experiment was made for the PU foam SikaBlock-M450 as well; the diameter of a sample was d_c = D_0 = 45 mm, and the thickness was t = 25 mm, as shown in Figure 3b.

2.7. Coverage Coefficients and the Corresponding Cylinders and Shells

Cylinders and shells of circular symmetry were used to study the partial susceptibility of rigid PU foams and monolithic polyurethanes, depending on the coverage coefficients of the active area of the OSA capacitive sensor. When a cylinder or a shell is placed concentrically on the circular active area, its coverage can be characterised by coverage coefficients k_c and k_s as follows:

$$\begin{gathered} k_c = \frac{S_c}{S_0} = \left(\frac{d_c}{D_0}\right)^2 = \left(\frac{r_c}{R_0}\right)^2, \\ k_s = \frac{S_s}{S_0} = \frac{\pi\left(D_0^2 - d_{sin}^2\right)}{\pi D_0^2} = 1.0 - \left(\frac{d_{sin}}{D_0}\right)^2 = 1.0 - \left(\frac{r_{sin}}{R_0}\right)^2,\ d_{sin} = d_{sout} - t, \\ 0.0 \le r_c,\ r_{sin} \le R_0 \text{ and } 0.0 \le k_c,\ k_s \le 1.0, \end{gathered} \tag{2}$$

where d_c—the diameter of the cylinder ($d_c \le D_0$), t—the thickness of the shell wall, d_{sin} and $d_{sout} = D_0 = 45$ mm—the inner and the outer diameters of the shell ($d_{sin} \le d_{sout}$), S_c—the cross-sectional area of a cylinder, S_s—the cross-sectional area of a shell and the total active area of the sensor, $S_0 = \pi/4{D_0}^2 = 1590.4$ mm^2.

A shell of outer diameter $d_{sout} = D_0 = 45$ mm and inner diameter d_{sin} is denoted as corresponding to a cylinder of diameter d_c, if $d_{sin} = d_c$. The summary cross-sectional area of a cylinder and a corresponding shell equals the sensor's active area, providing 100% coverage, Figure 4, as follows:

$$S_c + S_s = S_0 \text{ and } k_c + k_s = 1.0. \tag{3}$$

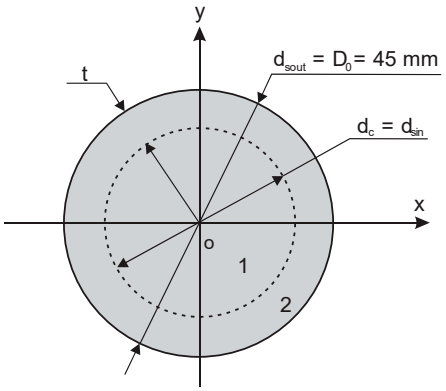


Figure 4. Cross-section of corresponding circular figures: cylinder 1 and shell 2.

The radius of a cylinder and the inner radius of a shell are related to the coverage coefficients k_c and k_s as follows:

$$r_c = 1/2D_0\sqrt{k_c} \text{ and } r_{sin} = 1/2D_0\sqrt{1 - k_{sin}}. \tag{4}$$

The dependence of k_c and k_s and their change rates $k_c' = \frac{dk_c}{dr_c} = \frac{2r_c}{R_0^2}$ and $k_s' = \frac{dk_s}{dr_{sin}} = -2\frac{r_{sin}}{R_0^2}$ on the radial dimension of the subsamples was evaluated.

2.8. The Measured Permittivity of Concentric Circular Subsamples

A complete cylindrical sample of PU foam SikaBlock-M240 (density of 230 kg/m^3, thickness t = 20 mm, diameter d = D_0 = 45 mm, and cross-sectional area S = S_0 = 1590.4 mm^2) was made, and its true permittivity was measured. The sample was cut into four concentric circular subsamples—a cylinder and three cylindrical shells, Figure 5. The dimensions of the subsamples were calculated to ensure an equal cross-sectional area S = $S_0/4$ = 397.6 mm^2, neglecting the finite width of the cutting lines. Then, the actual dimensions of the subsamples were measured, and the coverage coefficients were calculated. The measured permittivity ε_m was determined for each subsample. To estimate the impact of PU foams,

lost as sawdust, the four subsamples were put one into another to form a combined, quasi-complete sample, and its measured permittivity ε_m was determined.

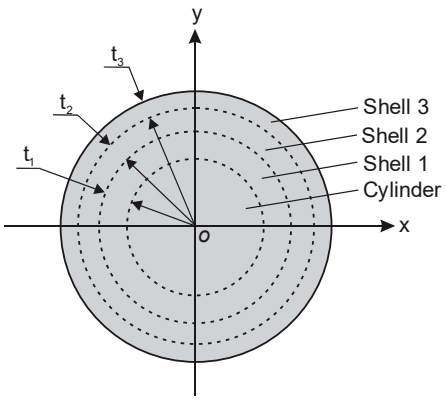


Figure 5. Cross-section of the concentric circular subsamples.

The true and the partial electric susceptibility χ_t and χ_p were calculated from experimental data of the true and the measured permittivity ε_t and ε_m.

2.9. The Measured Permittivity at a Partial Coverage

To study the partial electric susceptibility of rigid PU foams and monolithic polyurethanes, with a dependence on the coverage coefficients of the sensor, two identical right, circular, and cylindrical complete samples (i = 0 and j = 0, thickness t = 20 mm, and diameter D_0 = 45 mm) were made from each dielectric material, as shown in Figure 6.

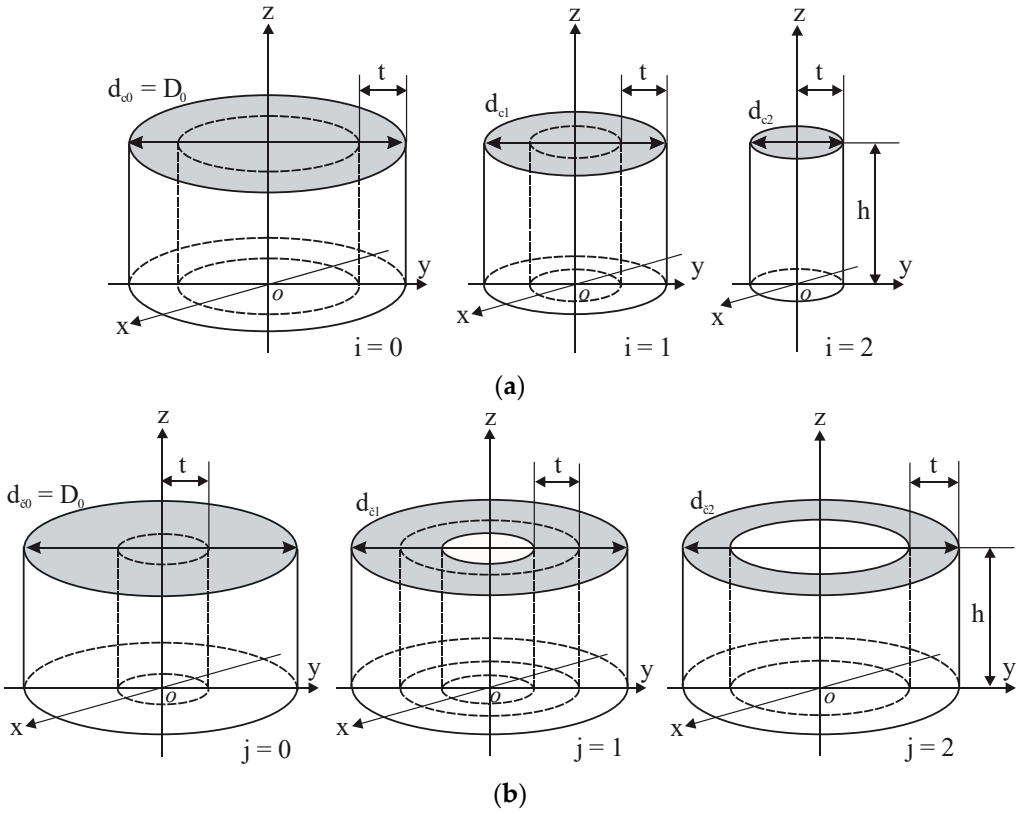


Figure 6. Complete samples (i = 0 and j = 0) and circular subsamples: (**a**) cylinders (i = 1 and 2) and (**b**) cylindrical shells (j = 1 and 2).

The true permittivity ε_t of both complete samples was measured. Then a concentric, circular, and cylindrical subsample (i = 1) was made by removing a shell of wall thickness

t from outside of the first complete sample, as in Figure 6a, and the measured permittivity of the subsample was determined. The next subsample (i = 2) was made, and its measured permittivity was determined, etc. A concentric, circular, and cylindrical shell was made by removing a cylinder of radius t from the centre of the second complete sample, as in Figure 6b, and the measured permittivity of the subsample j = 1 was determined, etc. Then the next shell (j = 2) was made by removing a shell of wall thickness t from the centre of the shell j = 1, and the permittivity of the shell, j = 2, was measured, etc. Altogether, 5 . . . 6 subsamples were made from each complete sample.

The measured permittivity of lab-made PU foams (density 32 and 78 kg/m^3) and industrial PU foam SikaBlock-M80 (85 kg/m^3), SikaBlock-M150 (144 kg/m^3), SikaBlock-M240 (226 kg/m^3), and SikaBlock-M450 (415 kg/m^3) was determined for cylinders. The measured permittivity of the shells was determined for light- to medium-weight PU foam SikaBlock-M80 (85 kg/m^3), SikaBlock-M150 (144 kg/m^3), and SikaBlock-M450 (415 kg/m^3).

The measured permittivity of monolithic dielectrics was determined for the cylinders, made of the lab-made monolithic polyurethane (1280 kg/m^3), the industrial monolithic polyurethane SikaBlock-M945 (1352 kg/m^3), and epoxy Lab-975New (708 kg/m^3). The shell-shaped subsamples of these high-density materials were not made due to technical challenges. The thickness of lab-made monolithic PU complete samples was t = 12 mm.

The spectrometer and the test materials were situated in the same premises for the entire study to attain thermodynamic equilibrium; no conditioning was made for the samples. The permittivity spectra were approximated according to methodology [8]. The true and the partial electric susceptibility, χ_t and χ_p, were calculated from experimental data of the true and the measured permittivity values, ε_t and ε_m, of the listed dielectric materials.

Data, corresponding to a frequency $f = 1/2(f_7 + f_8) = 960$ Hz ≈ 1 kHz, are given in this paper. For two density cases, (1) light-weight PU foam SikaBlock-M80 (85 kg/m^3) and (2) Monolithic PU SikaBlock-M945 (1352 kg/m^3) data, corresponding to f_{13} = 40,960 Hz, are given as well to evaluate the dielectric dispersion [26].

3. Theoretical

3.1. Model Functions

The true and the partial susceptibility of a dielectric material, χ_t and χ_p, are related to the true and the measured permittivity, ε_t and ε_m, as follows:

$$\chi_t = \varepsilon_t - 1.0 \text{ and } \chi_p = \varepsilon_m - 1.0. \quad (5)$$

The experimental data curves $\varepsilon_m = \varepsilon_m(r)$ of cylinders and shells were recalculated to $\chi_p = \chi_p(r)$, and the relative partial susceptibility RX was implemented by normalising the partial susceptibility $\chi_p(r)$ with χ_t:

$$RX(r_c) = \frac{\chi_{pc}(r_c)}{\chi_t} = \frac{\varepsilon_{mc}(r_c) - 1.0}{\varepsilon_t - 1.0} \text{ and } RX(r_{sin}) = \frac{\chi_{ps}(r_{sin})}{\chi_t} = \frac{\varepsilon_{ms}(r_{sin}) - 1.0}{\varepsilon_t - 1.0}, \quad (6)$$

where r_c or r_{sin} are the radiuses of cylinders and shells. With such a definition, RX characterises the fraction, which a subsample's partial susceptibility forms from the true susceptibility of a complete sample. The values of the relative partial susceptibility lie in a common scale of $0.0 \leq RX(r_c)$ and $RX(r_{sin}) \leq 1.0$. Analysis of calculated $RX(r_c)$ and $RX(r_{sin})$ data curves identified an inflection point at $r_{e2} < r_{infl} < r_{e1in}$, where r_{e1in} is the inner radius of the electrode №1 and r_{e2} is the radius of the electrode №2.

To model the calculated data curves $RX(r_c)$ and $RX(r_{sin})$, different functions were tested, but none of them described the relationships properly. Therefore, the model function is proposed as a combination of two normalized functions: (1) a cumulative normal

distribution and (2) a cumulative lognormal distribution. For cylinders, the model function $\Phi(r_c) \approx RX(r_c)$ equals the following:

$$\begin{aligned} f_1(r_c) &= \frac{1}{\sqrt{2\pi}\sigma_1}\int_0^{r_c} e^{-\frac{(r-\mu_1)^2}{2\sigma_1^2}}\,dr \text{ at } r_c < r_{infl} \text{ and} \\ f_2(r_c) &= \frac{1}{\sqrt{2\pi}\sigma_2 r_c}\int_{r_c}^{R_0} e^{-\frac{[\ln(r)-\mu_2]^2}{2\sigma_2^2}}\,dr \text{ at } r_c \geq r_{infl}, \end{aligned} \tag{7}$$

where parameters μ_1, μ_2 are mean values and σ_1, σ_2 are standard deviations. The functions $f_1(r_c)$ and $f_2(r_c)$ are joined at the intersection point, which coincides with the inflection point. To join $f_1(r_c)$ and $f_2(r_c)$ smoothly, their average value can be assigned to RX at the joining point, when necessary.

3.2. Change Rate of the Relative Partial Susceptibility

In order to characterise the change rate of the relative partial susceptibility RX, with a dependence on the radius of dielectric cylinders, $\Delta RX(r_c)/\Delta r_c$ can be estimated from the model function $\Phi(r_c)$ as follows:

$$\Delta RX(r_c)/\Delta r_c \approx \Delta\Phi(r_c)/\Delta r_c. \tag{8}$$

But, with an increase in the cylinder's radius r_c, the coverage coefficient k_c increases nonlinearly, as in Equation (2), and the increments of the coverage coefficient, which correspond to constant increments of radius Δr_c = const., are radius-dependent:

$$k_c{}' \approx \frac{\Delta k_c}{\Delta r_c} = \frac{2r_c}{R_0^2} \text{ and } \Delta k_c = 2r_c\frac{\Delta r_c}{R_0^2}. \tag{9}$$

Therefore, estimation (8) is not fit for the purpose, and the change rate of RX has to be determined at constant increments of the OSA sensor's coverage. Substituting $r_c = R_0\sqrt{k_c}$ into Equation (7), we obtain the following:

$$\Delta RX(k_c)/\Delta k_c \approx \Delta\Phi(k_c)/\Delta k_c. \tag{10}$$

This corresponds to a constant increase in the cross-sectional area of the cylinders: when Δk_c = const., then $\Delta S_c = S_0\Delta k_c$ = const., as shown in Equation (2).

Analysis of the calculated data curves $RX(r_c)$ and $RX(r_{sin})$ of low- to medium-density PU foams (85 kg/m^3, 144 kg/m^3, and 415 kg/m^3) identified a relationship between the relative partial susceptibilities of corresponding cylinders and shells:

$$RX(r_c) + RX(r_{sin}) = 1.0. \tag{11}$$

Then, taking into account $r_{sin} = r_c$ for the corresponding cylinders and shells, the model function for shells $\Psi(r_{sin}) \approx RX(r_{sin})$ can be constructed as follows:

$$\begin{aligned} f_3(r_{sin}) &= 1.0 - f_1(r_{sin}) = 1.0 - \frac{1}{\sqrt{2\pi}\sigma_1}\int_0^{r_{sin}} e^{-\frac{(r-\mu_1)^2}{2\sigma_1^2}}\,dr \text{ at } r_{sin} < r_{infl} \text{ and} \\ f_4(r_{sin}) &= 1.0 - f_2(r_{sin}) = 1.0 - \frac{1}{\sqrt{2\pi}\sigma_2 r_{sin}}\int_{r_{sin}}^{R_0} e^{-\frac{[\ln(r)-\mu_2]^2}{2\sigma_2^2}}\,dr \text{ at } r_{sin} \geq r_{infl}. \end{aligned} \tag{12}$$

For shells, constant increments of radius Δr_{sin} = const. provide radius-dependent increments of coverage coefficient k_s as follows:

$$k_s{}' \approx \frac{\Delta k_s}{\Delta r_{sin}} = -\frac{2r_{sin}}{R_0^2}, \text{ then } \Delta k_s = -2r_{sin}\frac{\Delta r_{sin}}{R_0^2}. \tag{13}$$

Therefore, the change rate of RX has to be estimated at constant increments of the OSA sensor's coverage with dielectric shells:

$$\Delta RX(k_s)/\Delta k_s \approx \Delta\Psi(k_s)/\Delta k_s. \quad (14)$$

A constant change in the cross-sectional area of a shell is ensured: when Δk_s = const., then $\Delta S_s = S_0 \Delta k_s$ = const., as shown in Equation (2). The $\Delta RX(k_s)/\Delta k_s$ curves for shells, cut from low- to medium-density PU foams (85 kg/m^3, 144 kg/m^3, and 415 kg/m^3), were calculated from model functions according to Equation (14).

Due to a lack of experimental data on the measured permittivity for shells of the high-density PU materials, the corresponding data curves $RX(r_{sin})$ could not be calculated. Consequently, Equation (14) could not be used to calculate the change rate of the relative partial susceptibility for shells, i.e., $\Delta RX(k_s)/\Delta k_s$. As an alternative, with $\Delta\Phi(k_c)/\Delta k_c$ known for cylinders, its relation to $\Delta\Psi(k_s)/\Delta k_s$ for shells was found. Taking into account $RX(r_c) \approx \Phi(r_c)$ and $RX(r_{sin}) \approx \Psi(r_{sin})$, we obtain the following from Equation (11):

$$\Phi(r_c) + \Psi(r_{sin}) = 1.0. \quad (15)$$

Substituting $r_c = R_0\sqrt{k_c}$ and $r_{sin} = R_0\sqrt{1.0 - k_s}$ into Equation (15) leads to the following:

$$\Phi(k_c) = 1.0 - \Psi(k_s). \quad (16)$$

Let us give both sides of Equation (16) a finite increment, $\Delta\Phi(k_c) = -\Delta\Psi(k_s)$, and then divide by Δk_c, $\frac{\Delta\Phi(k_c)}{\Delta k_c} = -\frac{\Delta\Psi(k_s)}{\Delta k_c}$. If the coverage coefficient of a cylinder increases, the coverage coefficient of the corresponding shell decreases for the same amount: $\Delta k_c = -\Delta k_s$. Then $\frac{\Delta\Phi(k_c)}{\Delta k_c} = \frac{\Delta\Psi(k_s)}{\Delta k_s}$, which permits us to calculate $\Delta\Psi(k_s)/\Delta k_s$ when $\Delta\Phi(k_c)/\Delta k_c$ is known.

In numerical calculations, the functions $f_1(r_c)$ and $f_2(r_c)$ were determined as normalised, cumulative standard functions NORMDIST(r_c, μ_1, σ_1, TRUE) and LOGNORM.DIST(r_c, μ_2, σ_2) of the MS EXCEL software v.12 (Microsoft Corporation; Redmond, WA, USA). A transformation of the radial coordinate $r_c' = r_c + r_T$ permitted us to translate the function $f_2(r_c)$ for a distance r_T to the best-fitting position. The parameters of $f_1(r_c)$ and $f_2(r_c)$, ensuring the best fitting of the calculated RX data, were determined for each dielectric material. Similar calculations were made for shells.

3.3. Increments of Radius at Constant Increments of Coverage Coefficient

To illustrate the distribution of the change rate of the relative partial susceptibility over the radius of the sensor's zone, covered with a dielectric cylinder, the curves "$\Delta RX(k_c)/\Delta k_c - k_c$" were recalculated to such r_c values, which correspond to constant increments of the coverage coefficient $\Delta k_c = k_{c(i+1)} - k_{ci}$ = const. Here "k_{ci}" and "$k_{c(i+1)}$" are points on the k_c − axis, i = 1, . . ., I + 1 and $I = k_c/\Delta k_c = 1.0/\Delta k_c$. Taking into account that $k_{ci} = (r_{ci}/R_0)^2$, the corresponding increments of the radius of a cylinder were calculated as follows:

$$\Delta r_{ci}(r_c) = -r_{ci} \pm \sqrt{r_{ci}^2 + R_0^2 \Delta k_c}, \text{ where } i = 1,\ 2,\ \ldots,\ I. \quad (17)$$

Since $r_c \geq 0.0$ mm for all 0.0 mm $\leq r_c \leq R_0$ mm, the positive square root is chosen. Then, the values of Δr_{ci} depend on r_c, but in a way that ensures Δk_c = const., as in Table 1. Similar calculations were made for the curves "$\Delta RX(k_s)/\Delta k_s - k_s$" in the case of shells.

Table 1. Increments of cylinder's radius Δr_c at a constant increment of the coverage coefficient Δk_c = 5%.

i	Coverage Coefficient k_c	Radius r_c; mm	Increment Δr_c; mm	i	Coverage Coefficient k_c	Radius r_c; mm	Increment Δr_c; mm
1	0.00	0.0	5.03	12	0.55	16.7	0.74
2	0.05	5.0	2.08	13	0.60	17.4	0.71
3	0.10	7.1	1.60	14	0.65	18.1	0.68

Table 1. *Cont.*

i	Coverage Coefficient k_c	Radius r_c; mm	Increment Δr_c; mm	i	Coverage Coefficient k_c	Radius r_c; mm	Increment Δr_c; mm
4	0.15	8.7	1.35	15	0.70	18.8	0.66
5	0.20	10.1	1.19	16	0.75	19.5	0.64
6	0.25	11.3	1.07	17	0.80	20.1	0.62
7	0.30	12.3	0.99	18	0.85	20.7	0.60
8	0.35	13.3	0.92	19	0.90	21.3	0.58
9	0.40	14.2	0.86	20	0.95	21.9	0.57
10	0.45	15.1	0.82	21	1.00	22.5	0.00
11	0.50	15.9	0.78				

Values of the change rate $\Delta RX(k_c)/\Delta k_c$ were calculated numerically at $\Delta k_c = 0.05$ (5%) for cylinders of PU materials with significantly differing permittivity.

4. Results and Discussion

4.1. Dielectric Losses

For PU foams with densities of 95–222 kg/m^3, dielectric losses were measured as $\varepsilon''(f) = 0.0022$–$0.0063$ (1 kHz) and $\varepsilon''(f) = 0.0032$–$0.0084$ (0.1 MHz). For monolithic lab-made polyurethane, $\varepsilon''(f) = 0.042$ at 1 kHz and $\varepsilon''(f) = 0.088$ at 0.1 MHz. The acquired data are in good correspondence with the experimental data in [26]. For the monolithic PU, $\varepsilon'(f) = 3.42$ (1 kHz) and the dielectric loss tangent $tg\delta = \varepsilon''(f)/\varepsilon'(f) = 0.012 << 1.0$. At higher frequencies of the considered range, f = 10 Hz–0.33 MHz, as in Equation (1), the dielectric losses are even smaller. The loss part of the PU materials, $\varepsilon''(f)$, is small compared to the real one, $\varepsilon'(f)$. Then $\widetilde{\varepsilon}(jf) \approx \varepsilon'(f)$, and the real part $\varepsilon'(f) = \varepsilon(f)$ is referred to as permittivity.

4.2. Lateral Dimensions of Complete Samples

For PU foams of densities 50–228 kg/m^3 and $\varepsilon_t = 1.14$–1.42 (1 kHz), the penetration depth was determined as 5.72 mm $\leq t_{3\%} \leq$ 5.87 mm $\pm$ 0.02 mm. That corresponds to the conclusions in [7]:, according to the definition of penetration depth, which is proposed in [7], the penetration depth of the OSA sensor increases as the permittivity of the sample increases. In order to achieve the same 3% difference, samples with high values of the true permittivity ε_t need to have a bigger penetration depth, $t_{3\%}$, whereas samples with low ε_t values can have smaller $t_{3\%}$ values to achieve the same percentage of difference [8]. The samples have to be thick enough to provide the true permittivity; therefore, 3–4 times the thickness of the penetration depth $t_{3\%}$ was taken as appropriate for PUR foams' samples with densities of 50–1280 kg/m^3 and t $\approx$ 20–25 mm [8]. Due to the limited dimensions of the lab-made monolithic PU rods, the semi-cylindrical samples were made with a thickness of 12 mm.

4.3. Transversal Dimensions of Complete Samples

The measured permittivity of PU foams and the expanded uncertainty U95% of the experimental data point are practically equal for all three considered kinds of samples: "(1)", "(2)", and "(3)". The differences lie in the limits of the uncertainty of the spectrometer $U_S95.45\% = \pm 0.01$, as shown in Table 2. No correlation was identified between the size/shape of the samples and the measured permittivity.

It is concluded that the measured permittivity ε_m, determined for parallelepiped-shaped samples, which ensure a 100% coverage of the sensor's active area, differs insignificantly from the true permittivity value ε_t, measured for complete cylindrical samples, exactly matching the sensor's active area. All three kinds of samples can be used to measure the true permittivity of PU foams.

Table 2. The measured permittivity and measurement uncertainties of PU foams.

N	Density ρ; kg/m^3	Kind of a Sample	Measured Permittivity ε_m			Expanded Uncertainty U95%		
			f_1	f_7	f_{16}	f_1	f_7	f_{16}
1	50	(1)	1.09	1.09	1.08	0.010	0.010	0.010
		(2)	1.10	1.09	1.08	0.010	0.010	0.010
		(3)	1.09	1.09	1.08	0.010	0.010	0.010
2	144	(1)	1.28	1.26	1.24	0.013	0.010	0.100
		(2)	1.27	1.26	1.25	0.012	0.010	0.100
		(3)	1.27	1.26	1.24	0.012	0.010	0.100
3	427	(1)	1.86	1.84	1.75	0.011	0.011	0.011
		(2)	1.87	1.84	1.76	0.015	0.011	0.010
		(3)	1.86	1.84	1.76	0.011	0.011	0.010

For the parallelepiped-shaped PU foam samples with a concentric cylindrical hole (D_0 = 45 mm), the readings of the spectrometer were equal to those acquired in measurements with no sample on the sensor ("Sensor in air"): $\varepsilon \approx 1.00 \pm 0.01$. PU foams, located outside the cylindrical zone above the active area of the sensor, have practically no effect on the measured permittivity value.

4.4. Inner Vertical Surfaces

For both PU materials, monolithic and cellular, the results at each frequency f_n (data at f_1 = 10 Hz, f_8 = 1280 Hz, and f_{16} = 327,680 Hz are displayed) showed a small relative difference between the permittivity of a complete cylindrical sample ε_t and the measured permittivity of two semi-cylindrical samples ε_{mc}: $R = (\varepsilon_t - \varepsilon_{mc})/\varepsilon_t$; $|R| < 0.5\%$, Table 3.

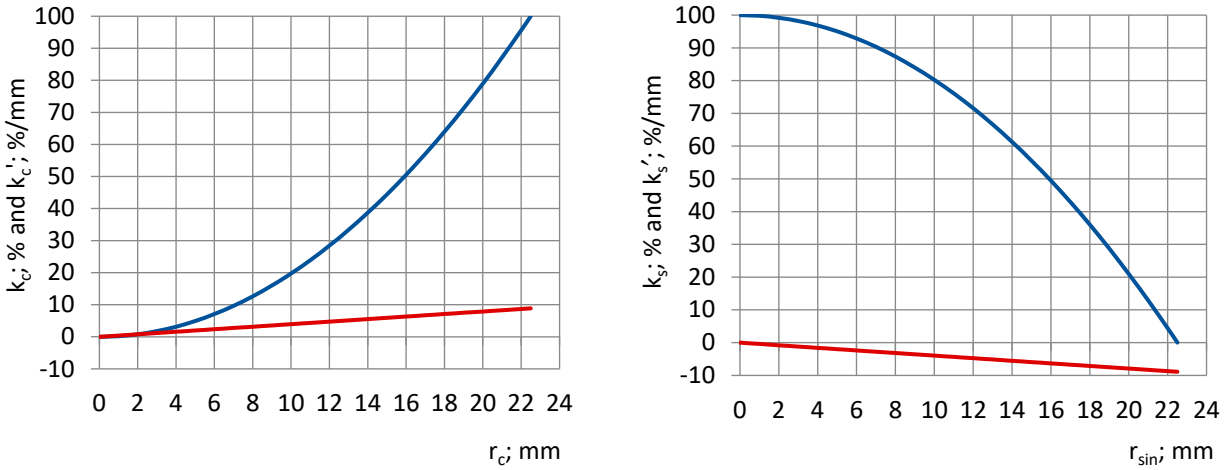
Table 3. The permittivity of cylindrical and semi-cylindrical samples.

N	Dielectric Material	Density ρ; kg/m^3	Sample	Thickness t; mm	Permittivity ε_t and ε_{mc}		
					f_1	f_8	f_{16}
1	PU foam SikaBlock-M450	437	A cylinder	12	1.855	1.802	1.756
2			Two semi-cylinders		1.852	1.804	1.757
		|R|; %			0.16	0.11	0.06
3	Monolithic PU SikaBlock- M960	1180	A cylinder	12	3.748	3.672	3.507
4			Two semi-cylinders		3.764	3.681	3.520
		|R|; %			0.43	0.25	0.37
5	Monolithic PU, lab-made	1280	Two semi-cylinders	12	3.474	3.408	3.310

It was concluded that a similar result could be expected for the lab-made monolithic PU as well. The inner vertical surfaces between the semi-cylinders have a negligible impact on the measured permittivity of a combined sample.

4.5. Coverage Coefficients

At an increase in the radius of the cylinders r_c and the inner radius of the shells r_{sin} from 0.0 mm to R_0 = 22.5 mm, the coverage coefficient of the cylinders k_c increases nonlinearly from 0% to 100%, while that of shells k_s decreases in the same way, as in Figure 7. The change rate k_c' increases linearly, and k_s' decreases by the same amount.



(**a**) (**b**)

Figure 7. Coverage coefficients k_c and k_s (blue) and their change rates k'_c and k'_s (red), depending on (**a**) the radiuses of the cylinders and (**b**) the inner radiuses of the shells.

4.6. The Measured Permittivity of Concentric Circular Subsamples

The theoretical parameters of the PU foam SikaBlock-M240 (230 kg/m^3) sample and subsamples are given in Table 4. The actual dimensions, in Table 5, can differ slightly. Around 5% of the cross-sectional area of a complete sample is changed into sawdust while cutting the three circular lines, each of width w ≈ 0.3 mm. As a result, the actual coverage coefficients k_c and k_s differ from those calculated with the assumption w = 0.0 mm.

Table 4. Theoretical parameters of the sample and subsamples (d_{in} and d_{out}—the inner and outer diameters).

Sample/Subsample	Diameter			Thickness of a Shell Wall t; mm	Cross-Sectional Area S; mm^2	Coverage Coefficients k_c and k_s; %
	d; mm	d_{in}; mm	d_{out}; mm			
Cylinder, complete	45.0	-	-	-	1590.4	100
Subsamples						
Cylinder	22.5	0.0	22.5	-	397.6	25
Shell 1	-	22.5	31.8	4.7	397.6	25
Shell 2	-	31.8	39.0	3.6	397.6	25
Shell 3	-	39.0	45.0	3.0	397.6	25
Sum:					1590.4	100
The combined sample						
Cylinder + shell 1 + shell 2 + shell 3	45.0	-		-	1590.4	100

Table 5. The parameters of the sample and subsamples, determined experimentally.

Sample/Subsample	Diameter			Thickness of a Shell Wall t; mm	Area S; mm^2	k_c and k_s; %	ε_t and ε_m (1 kHz)	Susceptibility χ_t and χ_p (1 kHz)	χ_p/Sumχ_p; %
	d; mm	d_{in}; mm	d_{out}; mm						
Cylinder, complete	44.9	-	-	-	1583.4	99.6	1.40	0.40	
Subsamples									
Cylinder	22.2	-	-	-	387.1	24.3	1.34	0.34	89.3
Shell 1	-	22.8	31.5	4.35	371.0	23.3	1.03	0.03	8.1
Shell 2	-	32.1	38.7	3.3	367.0	23.1	1.01	0.01	2.1
Shell 3	-	39.1	44.9	2.9	382.6	24.1	1.00	0.00	0.5
Sum:					1507.7	94.8	4.38	0.38	100.0
The combined sample									
Cylinder + shell 1 + shell 2 + shell 3	44.9	-	-	-	1507.7	94.8	1.40	0.40	100.0

Analysis of experimental data showed that the true permittivity of a complete cylindrical sample can be calculated from the measured permittivity of the four concentric circular subsamples, each of them covering the sensor's active area partially, as follows:

$$\varepsilon_t \approx \varepsilon' = \varepsilon_{mc} + \sum_{j=1}^{3} \varepsilon_{msj} - 3.0 = 1.38. \quad (18)$$

where ε_{mc} and ε_{ms} are the measured permittivities of the subsamples. The relative difference between the true permittivity of the complete cylinder and (1) the calculated permittivity ε' is estimated as $R_1 = (\varepsilon_t - \varepsilon')/\varepsilon_t = (1.40 - 1.38)/1.14 \approx 1.4\%$ and (2) the measured permittivity of the combined sample ε_m as $R_2 = (\varepsilon_t - \varepsilon_m)/\varepsilon_t < 1.0\%$. The true susceptibility χ_t of the complete cylindrical sample was determined from the calculated partial susceptibilities of the four concentric circular subsamples as follows:

$$\begin{array}{l} \chi_{pc} = \varepsilon_{mc} - 1.0;\ \chi_{ps} = \varepsilon_{ms} - 1.0, \text{ then} \\ \chi_t \approx \chi' = \chi_{pc} + \sum_{j=1}^{3} \chi_{psj} + 1.0 = 1.38. \end{array} \quad (19)$$

It can be seen that, although the subsamples have similar coverage coefficients $k_c \approx k_s$, the partial susceptibilities differ considerably, as shown in Table 5. The cylindrical subsample provides ~90% of the true susceptibility, while the three shells only ~10%, indicating an uneven distribution of the electric charge over the active area of the sensor. In a general case, for J subsamples (J − 1 shells and a cylinder), the following is calculated:

$$\varepsilon_t \approx \varepsilon' = \varepsilon_{mc} + \sum_{j=1}^{J-1} \varepsilon_{msj} - J \text{ and } \chi_t \approx \chi' = \chi_{pc} + \sum_{1}^{J-1} \chi_{ps} + 1.0. \quad (20)$$

4.7. The Measured Permittivity and the Partial Susceptibility at a Partial Coverage

4.7.1. PU Foams with Similar True Permittivity

The experimental data of the measured permittivity of low- to medium-density PU foams (32–415 kg/m^3), with similar true permittivity $1.00 < \varepsilon_t < 1.80$, are depicted in Figure 8 with a dependence on the radius of the cylinders.

At an increase of r_c from 0.0 mm to R_0 = 22.5 mm, the measured permittivity ε_{mc} increases from 0.0 to the value of the true permittivity ε_t. The concave–onvex curves "$\varepsilon_{mc} - r_c$" have inflection points, located at the limits of $r_{e2} \le r_c \le r_{e1in}$, where r_{e1in} is the inner radius of electrode №1, and r_{e2} is the radius of electrode №2. The dashed verticals in Figure 8 and other Figures mark the location of the radiuses r_{e1in} and r_{e2} of the sensor's electrodes №1 and №2 as well as the radius, r_{e3}, of the thickness centre of the guard electrode, as in Table 6. Coverage coefficients are given for cylinders in Table 6, when the radius of a cylinder $r_c = r_{e1in}$, $r_c = r_{e1out}$, $r_c = r_{e2}$, and $r_c = r_{e3}$, as well as for shells, when the inner radius of a shell $r_{sin} = r_{e1in}$, r_{sout}, $r_{sin} = r_{e2}$, and $r_{sin} = r_{e3}$.

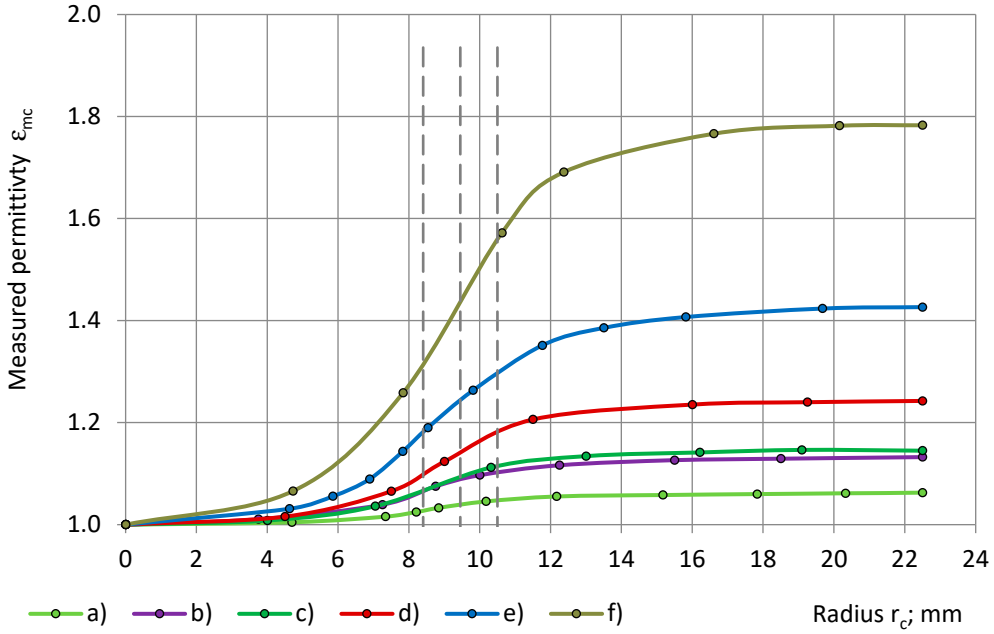


Figure 8. The measured permittivity ε_{mc} with a dependence on the cylinder's radius r_c: lab-made PU foams of density (**a**) 32 kg/m^3 and (**b**) 78 kg/m^3 and industrial PU foams (**c**) SikaBlock-M80 (85 kg/m^3), (**d**) SikaBlock-M150 (144 kg/m^3), (**e**) SikaBlock-M240 (226 kg/m^3), and (**f**) SikaBlock-M450 (415 kg/m^3) at f = 1 kHz.

Table 6. Radiuses of the sensor's electrodes and corresponding coverage coefficients for cylinders and shells.

Radius r_{e1in}; mm	**Coverage Coefficients k_c and k_s; %**	**Radius r_{e1out}; mm**	**Coverage Coefficients k_c and k_s; %**	**Radius r_{e2}; mm**	**Coverage Coefficients k_c and k_s; %**	**Radius r_{e3}; mm**	**Coverage Coefficients k_c and k_s; %**
10.50	21.8 / 78.2	22.50	100.0 / 0.0	8.40	13.9 / 86.1	9.45	17.6 / 82.4

The cross-sectional area of a cylinder increases, as its radius increases, from the centre of the cylinder to its outer perimeter. The cross-sectional area of a shell increases as the inner radius of the shell decreases, in the direction from the outer perimeter of the shell to its centre. The ring-shaped area between the electrodes №1 and №2 corresponds to ≈7.9% of the active area (for a cylinder 21.8% − 13.9% = 7.9% as well as for a shell, 86.1% − 78.2% = 7.9%).

Figure 9 gives experimental data of the measured permittivity ε_{mc} with a dependence on radiuses r_c and r_{sin} of the cylinders and shells.

The curves "$\varepsilon_{mc} - r_c$" and "$\varepsilon_{ms} - r_{sin}$ are symmetrical about a straight line, drawn parallel to the Or_c (Or_{sin}) axis and passing through the intersection point of the curves. Then, for each radius of a cylindrical subsample, 0.0 mm ≤ r_c ≤ 22.5 mm, the following relation holds:

$$\varepsilon_c(r_c) + \varepsilon_s(r_{sin}) = \varepsilon_t. \quad (21)$$

It can be seen that the true permittivity of PU foams can be determined as a sum of the measured permittivity of the corresponding circular subsamples: a cylinder and a shell. The intersection points of the curves practically coincide with the inflection points.

The transition to the calculated relative partial susceptibility RX, as in Equations (6), brings the experimental data from Figures 8 and 9 to a common scale of 0.0 ≤ RX(r_c) and RX(r_{sin}) ≤ 1.0, as in Figures 10 and 11.

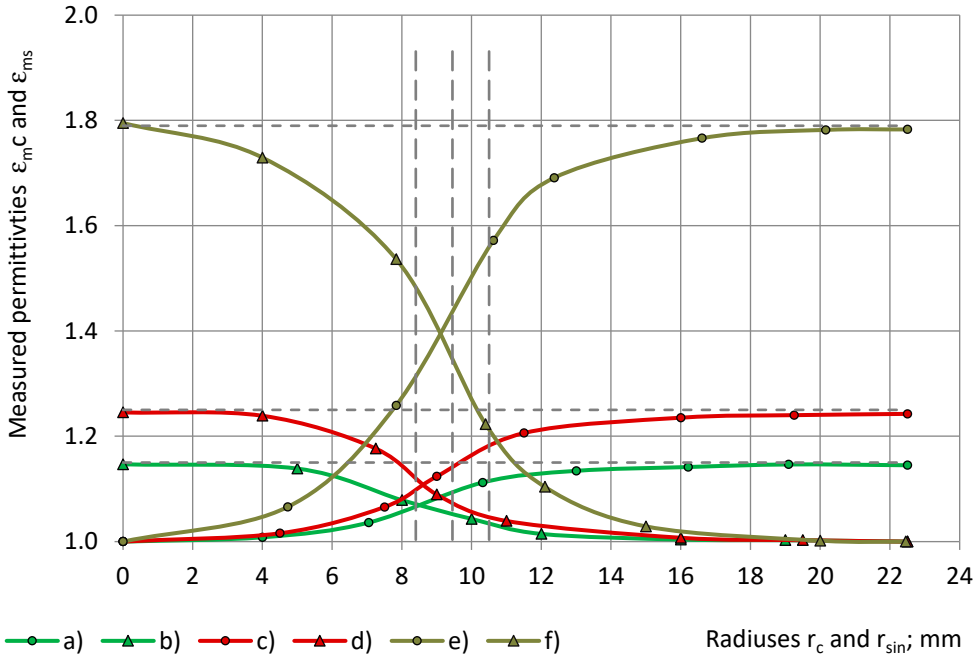


Figure 9. The measured permittivity ε_{mc} of PU foams' cylinders: (**a**,**c**,**e**) as well as ε_{ms} of shells: (**b**,**d**,**f**), with a dependence on the subsamples' radiuses r_c (circles) and r_{sin} (triangles). Densities: (**a**,**b**) SikaBlock-M80 (85 kg/m^3), (**c**,**d**) SikaBlock-M150 (144 kg/m^3), and (**e**,**f**) SikaBlock-M450 (415 kg/m^3) at f = 1 kHz.

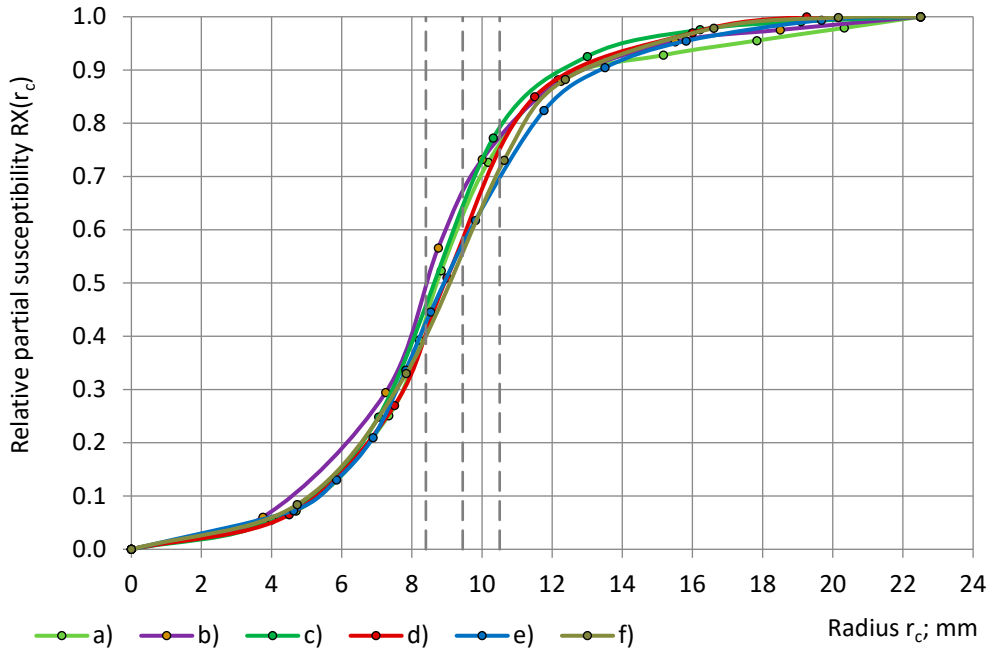


Figure 10. The relative partial susceptibility RX with a dependence on the cylinder's radius r_c: lab-made PU foams with densities of (**a**) 32 kg/m^3 and (**b**) 78 kg/m^3 and industrial PU foams (**c**) SikaBlock-M80 (85 kg/m^3), (**d**) SikaBlock-M150 (144 kg/m^3), (**e**) SikaBlock-M240 (226 kg/m^3), and (**f**) SikaBlock-M450 (415 kg/m^3) at f = 1 kHz.

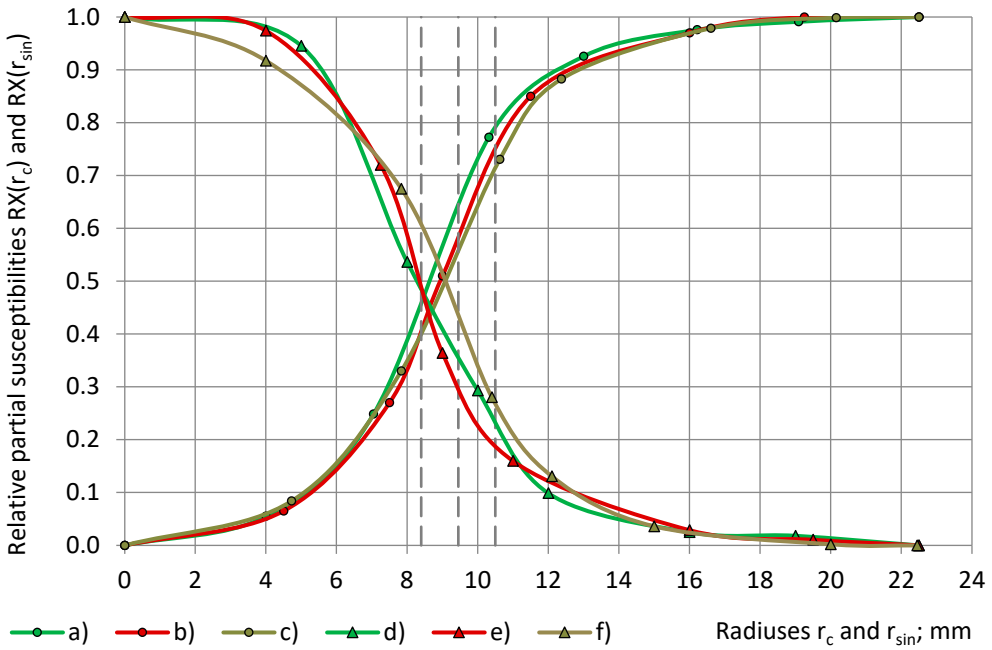


Figure 11. The relative partial susceptibility RX of PU foams' cylinders (**a**,**c**,**e**) as well as of the corresponding shells (**b**,**d**,**f**) with a dependence on the subsamples' radiuses r_c (circles) and r_{sin} (triangles). Densities: (**a**,**d**) SikaBlock-M80 (85 kg/m^3), (**b**,**e**) SikaBlock-M150 (144 kg/m^3), and (**c**,**f**) SikaBlock-M450 (415 kg/m^3) at f = 1 kHz.

The parameters of the best-fitting model functions $\Phi(r_c)$ and $\Psi(r_{sin})$ of the calculated relationships "$RX(r_c) - r_c$" and "$RX(r_{sin}) - r_{sin}$" are given in Table 7. Theoretically, the parameters of $\Psi(r_{sin})$ have to be the same as those of $\Phi(r_c)$, as in Equations (7) and (10), but practically, they can differ due to irregularities in the subsamples' shape, density, etc. For PU foams of a similar true permittivity, $1.00 < \varepsilon_t < 1.80$, the curves "$RX(r_c) - r_c$" and "$RX(r_{sin}) - r_{sin}$" have a similar shape, are close together, and partially overlap, as in Figures 10 and 11, which hinders the determination of the parameters and the identification of the main trends.

Table 7. Parameters of the model functions $\Phi(r_c)$ and $\Psi(r_{sin})$ for cylinders and shells.

N	PU Foams	Density ρ; kg/m^3	True Permitt. ε_t (1 kHz)	Model Functions $\Phi(r_c)$ and $\Psi(r_{sin})$					
				Normal Cumulative $f_{1c}(r_c)$ or $f_{1s}(r_{sin})$			Lognormal Cumulative $f_{2c}(r_c)$ or $f_{2s}(r_{sin})$		
				μ_1	σ_1	Logical	μ_2	σ_2	r_T
			Cylinders						
1	SikaBlock-M80	85	1.15	8.8	2.9	TRUE	1.32	0.56	−4.8
2	SikaBlock-M150	144	1.24	9.0	2.8	---"---	1.29	0.59	−5.1
3	SikaBlock-M450	415	1.78	9.1	3.1	---"---	1.32	0.57	−5.3
			Shells						
1	SikaBlock-M80	85	1.15	8.8	2.9	TRUE	1.32	0.56	−4.8
2	SikaBlock-M150	144	1.24	9.0	2.7	---"---	1.10	0.67	−5.3
3	SikaBlock-M450	415	1.78	9.1	3.1	---"---	1.32	0.57	−5.3

It can be seen that the model curves "$\Phi(r_c) - r_c$" and "$\Psi(r_{sin}) - r_{sin}$" for cylinders and shells of both PU foams are symmetrical about a straight line, which is drawn parallel to the Or_c (Or_{sin}) axis and passes through the intersection of the curves at $\Phi(r_c) = \Psi(r_{sin}) = 50\%$, as in Figure 12. Then, for each radius of a cylinder, 0.0 mm $\leq r_c \leq$ 22.5 mm, and the radius of the cylinder's corresponding shell, $r_{sin} = r_c$, the following hold:

$$\Phi(r_c) + \Psi(r_{sin}) = 1.0 \text{ and } RX(r_c) + RX(r_{sin}) = 1.0. \quad (22)$$

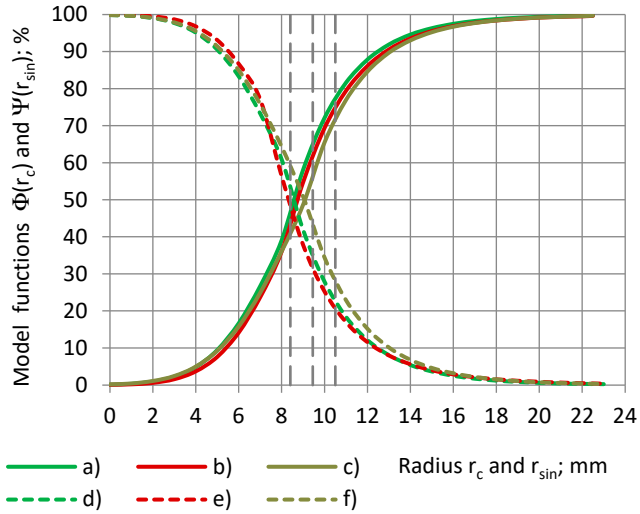


Figure 12. Model functions Φ and Ψ of the relative partial susceptibility RX of PU foams' cylinders (**a**–**c**) as well as of the corresponding shells (**d**–**f**) with a dependence on the radiuses of subsamples r_c and r_{sin}. Densities: (**a**,**d**) SikaBlock-M80 (85 kg/m^3), (**b**,**e**) SikaBlock-M150 (144 kg/m^3), and (**c**,**f**) SikaBlock-M450 (415 kg/m^3) at f = 1 kHz.

For each cylinder of a coverage coefficient k_c 0.0% ≤ k_c ≤ 100% and the cylinder's corresponding shell of a coverage coefficient k_s, k_c + k_s = 100% is valid, as shown in Equation (3). Then, from Figure 13 we obtain the following:

$$\Phi(k_c) + \Psi(k_s) = \Phi(k_c) + \Psi(100\% - k_c) = 100\%. \quad (23)$$

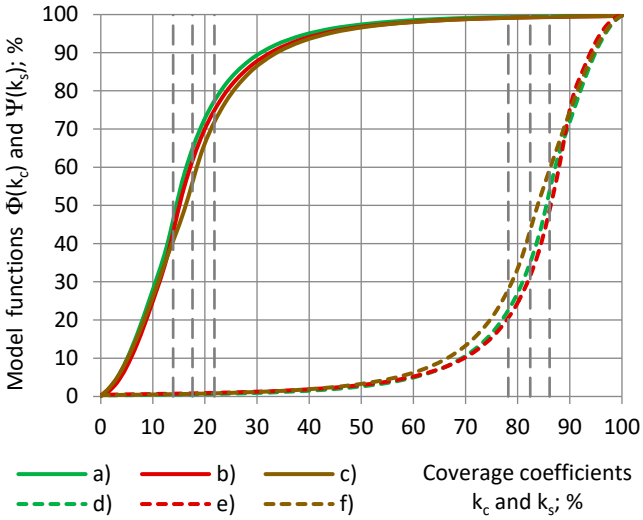


Figure 13. Model functions Φ and Ψ of the relative partial susceptibility RX of PU foams' cylinders (**a**–**c**) as well as of the corresponding shells (**d**–**f**) with a dependence on the coverage coefficients k_c and k_s. Densities: (**a**,**d**) SikaBlock-M80 (85 kg/m^3), (**b**,**e**) SikaBlock-M150 (144 kg/m^3), and (**c**,**f**) SikaBlock-M450 (415 kg/m^3) at f = 1 kHz.

4.7.2. PU Materials with Significantly Differing True Permittivity

The experimental data of the measured permittivity of dielectrics (PU foams, monolithic polyurethane, and an epoxy) with significantly differing true permittivity (1.0 < ε_t < 9.0) are given in Figure 14 with a dependence on the radius of the cylinders. With an increase of r_c from 0.0 mm to R_0 = 22.5 mm, the measured permittivity ε_{mc} increases from 0 to ε_t.

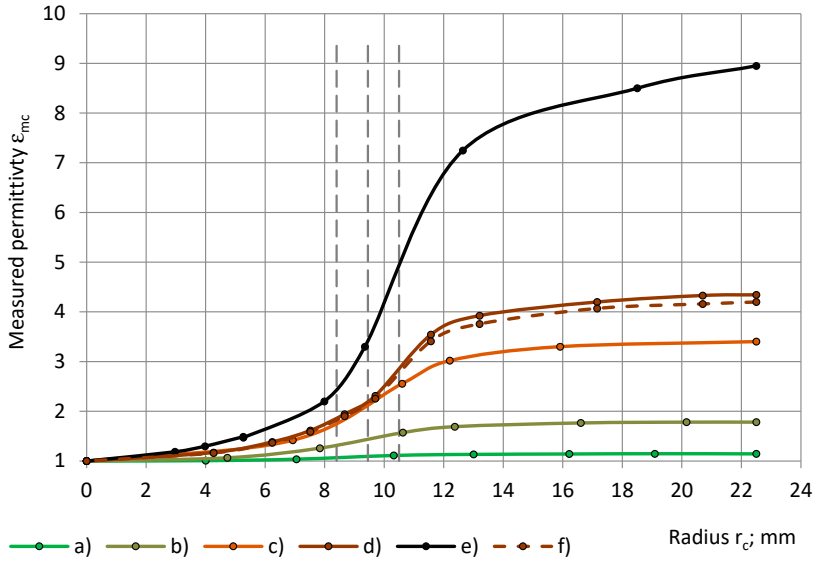


Figure 14. The measured permittivity ε_{mc} with a dependence on the cylinder's radius r_c: PU foams (**a**) SikaBlock-M80 (85 kg/m^3), (**b**) SikaBlock-M450 (415 kg/m^3), monolithic materials, (**c**) lab-made PU (1280 kg/m^3), (**d**) industrial PU SikaBlock-M945 (1352 kg/m^3), (**e**) industrial epoxy Lab-975 New (708 kg/m^3) at f = 1 kHz, and (**f**) industrial PU SikaBlock-M945 (1352 kg/m^3) at f = 40960 Hz.

The $\varepsilon_m = \varepsilon_m(r_c)$ curves, registered for the light-weight PU foam SikaBlock-M80 (85 kg/m^3) at frequencies 1000 Hz and 40,960 Hz, practically overlap, because the differences $\Delta\varepsilon_m$ between the ε_m values at both frequencies are less than 0.001. For the monolithic polyurethane SikaBlock-M945 (1352 kg/m^3), the $\varepsilon_m = \varepsilon_m(r_c)$ curve at 40,960 Hz is given in Figure 14f and $\Delta\varepsilon_m < 0.20$. When the $\varepsilon_m = \varepsilon_m(r_c)$ curves are recalculated to the relative partial susceptibility RX, as in Equations (5) and (6), the RX = RX(r_c) curves at 1000 Hz and 40960 Hz coincide closely for both PU materials and provide no new information. Therefore, the curves RX = RX(r_c) at f_{13} = 40,960 Hz are not depicted in Figure 15. It is reasonable to expect the same for PU foams of density values below the density of monolithic PU SikaBlock-M945. It is concluded that the studied PU materials exhibit low dielectric dispersion.

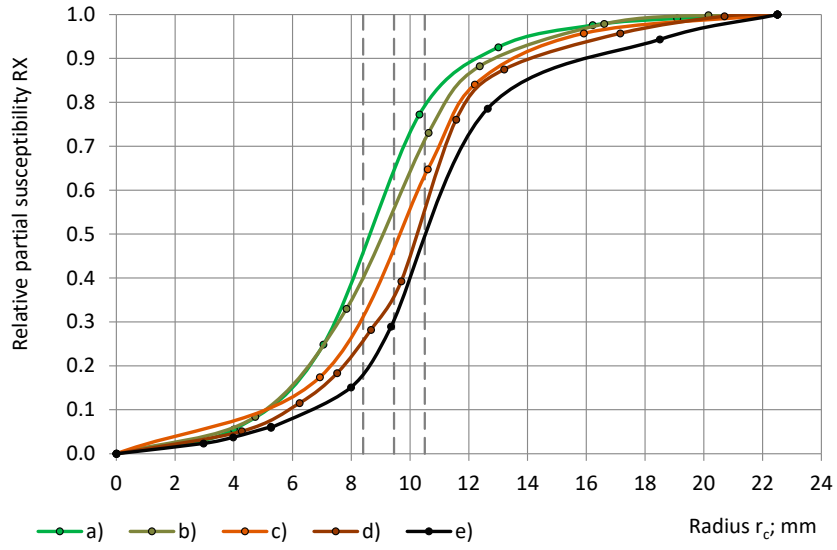


Figure 15. The relative partial susceptibility RX with a dependence on the cylinder's radius r_c: (**a**) SikaBlock-M80 (85 kg/m^3), (**b**) PU foam SikaBlock-M450 (415 kg/m^3), monolithic materials, (**c**) lab-made PU (1280 kg/m^3), (**d**) industrial PU SikaBlock-M945 (1352 kg/m^3), and (**e**) industrial epoxy Lab-975 New (708 kg/m^3) at f = 1 kHz.

The calculated data curves of the relative partial susceptibility $RX(r_c)$ follow a similar, concave/convex pattern, with inflection points at the limits, $r_{e2} \leq r_c \leq r_{e1in}$, as in Figure 15. For dielectrics with higher true permittivity, the inflection points correspond to higher values of the radius of the cylinders, r_c.

The ε_t values of the considered dielectrics are sufficiently different to prevent overlapping of the curves $RX(r_c)$ and to facilitate a determination of the main trends and parameters of model functions, as shown in Table 8.

Table 8. The parameters of model function $\Phi(r_c)$ (cylinders).

N	Dielectric Material	Density; kg/m^3	Permitt. ε_t (1 kHz)	Model Function $\Phi(r_c)$					
				Normal Cumulative $f_1(r_c)$			Lognormal Cumulative $f_2(r_c)$		
				μ_1	σ_1	Logical	μ_2	σ_2	r_T
1	Monolithic PU; lab-made	1280	3.40	9.8	3.5	TRUE	1.30	0.58	−6.0
2	Monolithic PU Sika M945	1352	4.34	10.8	3.6	---"---	1.15	0.63	−7.0
3	Epoxy LAB975	708	8.95	12.0	4.0	---"---	1.10	0.73	−7.6

The main features of the calculated data curves $RX(r_c)$, as in Figure 15, are valid for the model functions $\Phi(r_c)$ of the relative partial susceptibility as well, as in Figure 16. Compared to the PU foam SikaBlock-M80 ($\varepsilon_t = 1.15$), the inflection point of the $\Phi = \Phi(r_c)$ curve for epoxy LAB975 ($\varepsilon_t = 8.95$) is located ≈2 mm further in the direction of the higher values of r_c. This can be explained by a higher input of the outer circular zones (covered with the dielectric) of the electrode №1 into the total transcapacitance. At higher values of the true permittivity, the input becomes sufficient to be detected by a spectrometer of a certain sensitivity.

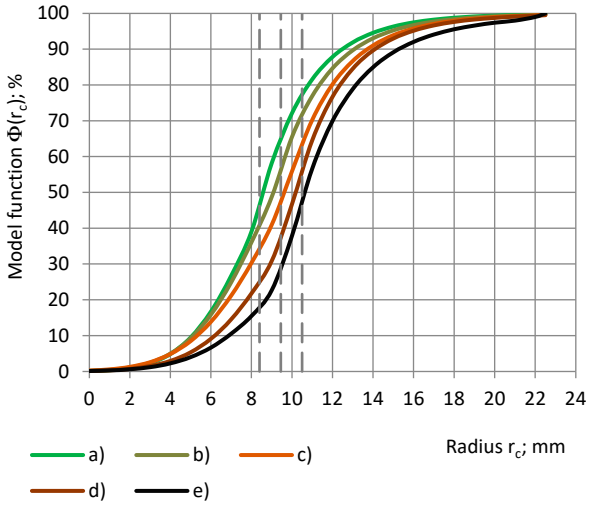


Figure 16. Model functions Φ of the relative partial susceptibility RX with a dependence on the cylinder's radius r_c: (**a**) SikaBlock-M80 (85 kg/m^3), (**b**) PU foam SikaBlock-M450 (415 kg/m^3), monolithic materials, (**c**) lab-made PU (1280 kg/m^3), (**d**) industrial PU SikaBlock-M945 (1352 kg/m^3), and (**e**) an epoxy Lab-975 New (708 kg/m^3) at f = 1 kHz.

For PU foams with densities of 78–85 kg/m^3, the true permittivity $1.13 \leq \varepsilon_t \leq 1.15$ is only ≈13–15% higher than that of vacuum $\varepsilon_{t0} = 1.0$. The outer circular zones of the electrode №1 ($r_c > 12 \ldots 15$ mm) have a lower charge density, compared to that of the inner zones [2]; as a result, their input is comparatively small.

The higher the true permittivity, the higher the coverage coefficient, at which a certain value of the relative partial susceptibility RX is reached: (a) 50%, (b) 75%, and (c) 90%, as in Figure 17.

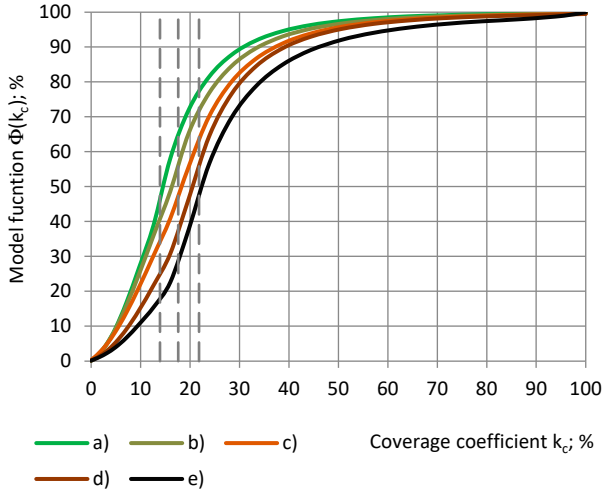


Figure 17. Model functions Φ of the relative partial susceptibility RX with a dependence on the coverage coefficient k_c of the cylinders: (**a**) SikaBlock-M80 (85 kg/m^3), (**b**) PU foam SikaBlock-M450 (415 kg/m^3), monolithic materials, (**c**) lab-made PU (1280 kg/m^3), (**d**) industrial PU SikaBlock-M945 (1352 kg/m^3), and (**e**) an epoxy Lab-975 New (708 kg/m^3) at f = 1 kHz.

The mentioned trend is displayed in Figure 18.

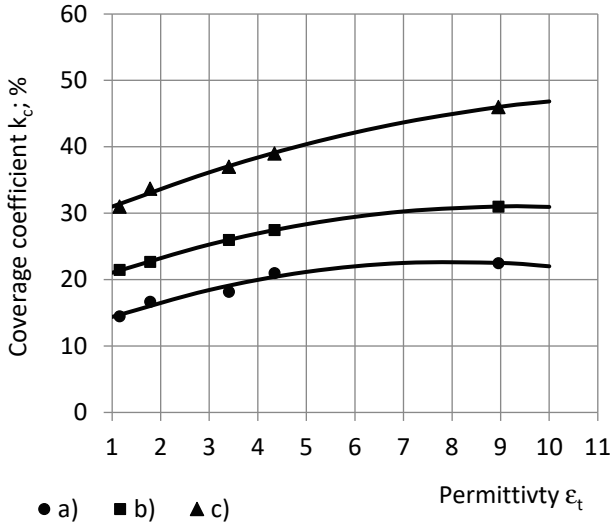


Figure 18. The dependence of the coverage coefficient k_c on the true permittivity ε_t at the relative partial susceptibility RX (**a**) 50%, (**b**) 75%, and (**c**) 90%.

This may be explained by a higher input of the outer circular zones of electrode №1 into the total transcapacitance, when at a higher true permittivity, the input becomes sufficient to be detected by a spectrometer of a certain sensitivity.

The coverage of the sensor's active area increases from 0% to 100% in the direction from (1) the centre to the perimeter at an increase of a cylinder's radius from 0 to R_0, and when $\Delta r_c > 0$, then $\Delta k_c > 0$, and in the direction from (2) the perimeter to the centre at a decrease of a shell's inner radius from R_0 to 0, and when $\Delta r_{sin} < 0$, then $\Delta k_s > 0$. The values of the change rate $\Delta RX(k_c)/\Delta k_c$ were calculated numerically at $\Delta k_c = \Delta k_s = 0.05$ (5%).

In the centre of the OSA sensor, in Figure 19, at $k_c = 0\%$ for cylinders, the change rate is $\Delta RX/\Delta k_c \approx$ 4–10%/5%, because the change rate value $\Delta RX/\Delta k_c$, calculated for each coverage interval $\Delta k_c = k_{c(i+1)} - k_{ci} = 5\%$, is assigned to its left point k_{ci}. $\Delta RX/\Delta k_c$ has the highest values of 20–25%/5% at 14% < k_c < 22%, which corresponds to the zone between electrodes №1 and №2. In the centre of the sensor, $\Delta RX/\Delta k_c$ is 2–5 times smaller, and it decreases to < 5%/5% as k_c increases above 35%. For shells, in the centre of the OSA sensor

at k_s = 100%, the corresponding value of the change rate $\Delta RX/\Delta k_s \approx$ 4–10%/5% is assigned to the right point of each Δk_s interval. $\Delta RX/\Delta k_s$ has the highest values of 20–25%/5% at 78% < k_s < 86% and decreases to less than 5%/5% at k_s < 65%, as shown in Table 6.

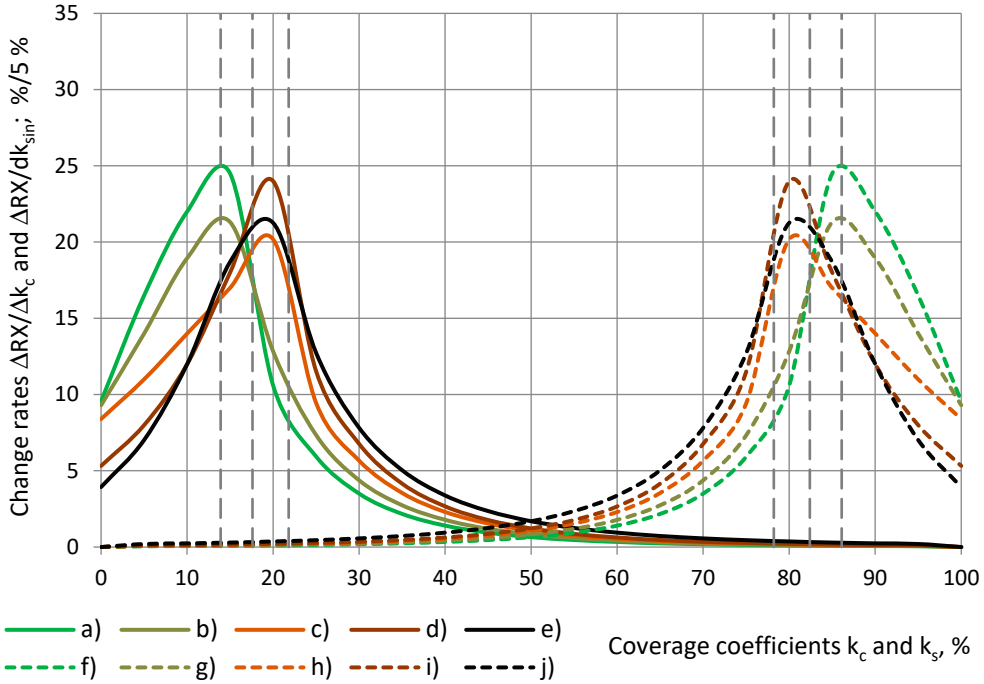


Figure 19. The change rate of the relative partial susceptibility, with a dependence on the coverage coefficient of the cylinders (continuous lines) and of shells (dashed lines): (**a**,**f**) SikaBlock-M80 (85 kg/m^3), (**b**,**g**) PU foam SikaBlock-M450 (415 kg/m^3), monolithic materials (**c**,**h**) lab-made PU (1280 kg/m^3), (**d**,**i**) industrial PU SikaBlock-M945 (1352 kg/m^3) as well as (**e**,**j**) an epoxy Lab-975 New (708 kg/m^3) at f = 1 kHz.

Figure 20 shows the change rate of the relative partial susceptibility $\Delta RX/\Delta k_c$ over the radius of the sensor's circular concentric zone, which is covered with a dielectric cylinder of radius r_c. The increments Δr_{ci}, corresponding to the markers on the curves, depend on r_c in a way that ensures constant increments of the coverage coefficient Δk_c = 5%, as in Equation (17). It can be seen that the change rate is the highest, $\Delta RX/\Delta k_c$ = 20–25%/5%, in the ring-shaped zone of radius 8.4 mm < r_c < 10.5 mm between electrodes №1 and №2. In the centre of the sensor, the change rate is 2–5 times smaller. As the radius r_c increases above 12 mm, $\Delta RX/\Delta k_c$ decreases to <5%/5%.

The numerical results of several mathematical models of other authors are available for circular OSA sensors with two electrodes in [2,7,13,15]. The overall character of the curves in Figure 20 like slopes of lines and the ratio of $\Delta RX/\Delta k_c$ values in the centre and near the gap corresponds with the character of the surface charge density distribution curves, calculated from mathematical modelling. In [11], a simplification is made by assuming an even distribution of the surface charge on the sensor's electrodes. In [12,13], a complex mathematical model for a circular three-electrode OSA sensor is elaborated, but numerical results for the surface charge are not displayed.

A shortage of experimental data for the surface charge density distribution over the active area of circular OSA sensors hinders a relevant comparison.

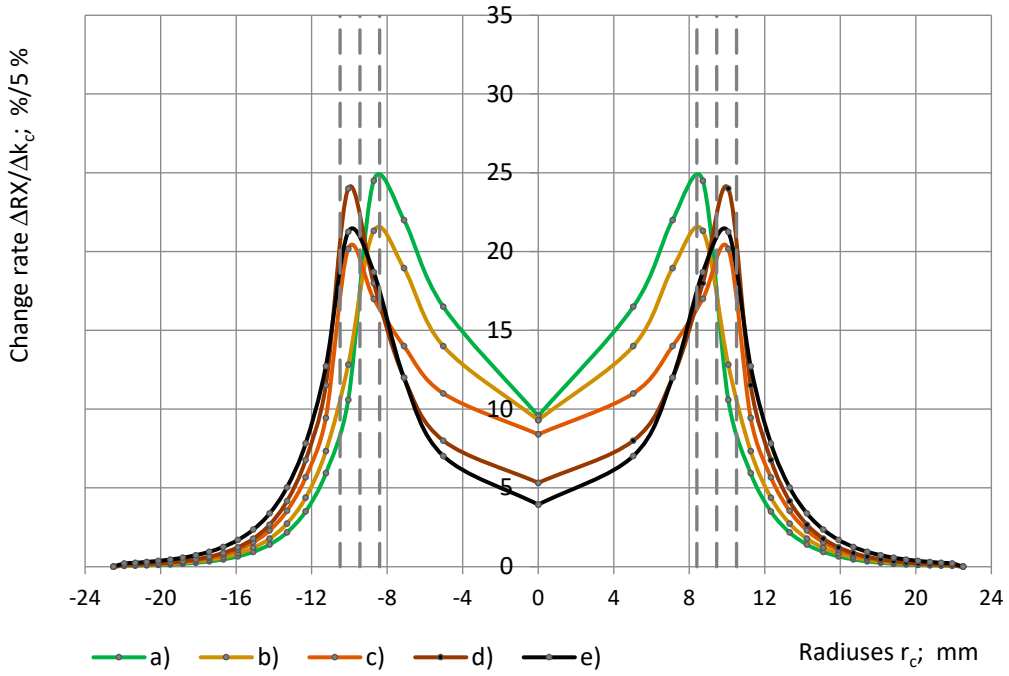


Figure 20. The change rate of the relative partial susceptibility $\Delta RX/\Delta k_c$ with a dependence on the radius r_c of a cylinder: (**a**) SikaBlock-M80 (85 kg/m^3), (**b**) PU foam SikaBlock-M450 (415 kg/m^3), monolithic materials, (**c**) lab-made PU (1280 kg/m^3), (**d**) industrial PU SikaBlock-M945 (1352 kg/m^3), as well as (**e**) an epoxy Lab-975 New (708 kg/m^3) at f = 1 kHz.

5. Conclusions

The electric susceptibility at the partial coverage of a circular OSA sensor with cylinders and shells is investigated for PU foams and monolithic polyurethane. It is shown experimentally that the true susceptibility can be determined from the partial susceptibilities of the corresponding subsamples. The implementation of the relative partial susceptibility permitted us to transform the calculated susceptibility data to a common scale of 0.0–1.0 and to outline the main trends for PU materials.

The partial susceptibility, the relative partial susceptibility, and the change rate of the relative partial susceptibility exhibit a marked dependence on the coverage coefficient of the OSA sensor's active area as well as a correlation with the coordinates of the sensor's electrodes and the gap. Numerical calculations showed that, for cylindrical subsamples, the change rate of the relative partial susceptibility is the highest in the zone of the active area between electrodes №1 and №2: 20–25%/5%. In the centre of the sensor, it is 2–5 times smaller and decreases below 5%/5% as the coverage coefficient increases above 35% in correspondence with the surface charge density distribution, reported in scientific information sources. The curves for shells are symmetric to those for the cylinders with respect to the location of the gap. The overall pattern of curves for the change rate of the relative partial susceptibility, characterised by slopes of lines and the ratio of $\Delta RX/\Delta k_c$ values in the centre and values near the gap, corresponds with the character of the surface charge density distribution curves, calculated from mathematical models.

The uncertainty of the spectrometer, geometric irregularities of subsamples, and varying humidity of the ambient atmosphere can be named as the main sources of measurement uncertainties for PU foams. The elaborated methods can be applied in the design and optimization of capacitive OSA sensors of other configurations of electrodes, independent of the particular technical solution.

Funding: This research received no external funding.

Institutional Review Board Statement: Not applicable.

Informed Consent Statement: Not applicable.

Data Availability Statement: Data are contained within this article.

Conflicts of Interest: The author declares no conflicts of interest.

References

1. Kremer, F.; Schonhals, A. (Eds.) *Broadband Dielectric Spectroscopy*; Springer: Berlin/Heidelberg, Germany, 2003; 730p. [CrossRef]
2. Matiss, I. *Capacitive Transducers for Non-Destructive Testing*; Zinatne: Riga, Latvia, 1982; 302p. (In Russian)
3. Kalpinsh, A.; Shtrauss, V.; Lomanovskis, U. Digital Emulation of Dielectric Relaxation Functions for Capacitive Sensors of Non-Destructive Dielectric Spectrometry. *Comput. Methods Exp. Meas.* **2019**, *125*, 111–119. [CrossRef]
4. Baxter, L.K. *Capacitive Sensors: Design and Applications*; Wiley Institute IEEE Press, Inc.: New York, NY, USA, 1997; 277p, 302p with Appendices.
5. Fraden, J. *Handbook of Modern Sensors*, 4th ed.; Springer: Berlin/Heidelberg, Germany, 2010; 663p. [CrossRef]
6. Chen, T.; Bowler, N. Analysis of a concentric coplanar capacitive sensor for nondestructive evaluation of multi-layered dielectric structures. *IEEE Trans. Dielectr. Electr. Insul.* **2010**, *17*, 1307–1318. [CrossRef]
7. Chen, T. Capacitive Sensors for Measuring Complex Permittivity of Planar and Cylindrical Structures. Ph.D. Thesis, Iowa State University, Ames, IA, USA, 2012. Available online: https://lib.dr.iastate.edu/etd/12294 (accessed on 11 March 2024).
8. Beverte, I.; Cabulis, U.; Gaidukovs, S. Polytetrafluoroethylene Films in Rigid Polyurethane Foams' Dielectric Permittivity Measurements with a One-Side Access Capacitive Sensor. *Polymers* **2021**, *13*, 1173. [CrossRef] [PubMed]
9. Chen, T.; Bowler, N. Analysis of concentric coplanar capacitor for quantitative dielectrometry. *Stud. Appl. Electromagn. Mech.* **2010**, *33*, 61–68. [CrossRef]
10. Chen, T.; Song, J.M.; Bowler, J.R.; Bowler, N. Analysis of a concentric coplanar capacitive sensor using a spectral domain approach. *Rev. Prog. Quant. Nondestr. Eval.* **2011**, *30*, 1647–1654.
11. Cheng, H.; Zhang, Y.; Huang, X.; Rogers, J.A.; Huang, Y. Analysis of a concentric coplanar capacitor for epidermal hydration sensing. *Sens. Actuator A Phys.* **2013**, *203*, 149–153. [CrossRef]
12. Sheiretov, Y. Deep Penetration Magnetoquasistatic Sensors. Ph.D. Thesis, Massachusetts Institute of Technology, Cambridge, MA, USA, 2001. Available online: https://web.mit.edu/yksheire/www/thesis.pdf (accessed on 11 March 2024).
13. Shay, I.C.; Zahn, M. Cylindrical geometry electroquasistatic dielectrometry sensors. *IEEE Trans. Dielectr. Electr. Insul.* **2005**, *12*, 41–49. [CrossRef]
14. Sheiretov, Y.; Zahn, M. Modeling of spatially periodic dielectric sensors in the presence of a top ground plane bounding the test dielectric. *IEEE Trans. Dielect. Electr. Insul.* **2005**, *5*, 993–1004. [CrossRef]
15. Bowler, N.; Chen, T. Concentric Coplanar Capacitive Sensor System with Quantitative Model. Patent US 8791707 B2, 29 July 2014.
16. Chu, Z.; Peng, C.; Ren, R.; Ling, B.; Zhang, Z.; Lei, H.; Xia, S. A High Sensitivity Electric Field Microsensor Based on Torsional Resonance. *Sensors* **2018**, *18*, 286. [CrossRef] [PubMed]
17. Guo, J.; Hu, P.; Tan, J. Annular Coplanar Capacitive Tilt Sensor. *Sensors* **2016**, *16*, 133. [CrossRef] [PubMed]
18. Hu, X.; Yang, W. Planar capacitive sensors–designs and applications. *Sens. Rev.* **2010**, *30*, 24–39. [CrossRef]
19. Gong, Y.; Zhu, H.; Li, N. Research on Coplanar Capacitive Sensor Design for Film Thickness Measurement. *Adv. Mater. Res.* **2014**, *945–949*, 2030–2036. [CrossRef]
20. Zaitsev, I.O.; Levytskyi, A.S. Determination of response characteristic of capacitive coplanar air gap sensor. In Proceedings of the 5th IEEE Microwaves, Radar and Remote Sensing Symposium, Kyiv, Ukraine, 29–31 August 2017. article number 8075034, code 131255. [CrossRef]
21. Zaitsev, I.O.; Levytskyi, A.S.; Novik, A.I.; Bereznychenko, V.O.; Smyrnova, A.M. Research of a capacitive distance sensor to grounded surface. *Telecommun. Radio Eng. Elektrosvyaz Radiotekhnika* **2019**, *78*, 173–180. [CrossRef]
22. Abdollahi-Mamoudan, F.; Savard, S.; Ibarra-Castanedo, C.; Filleter, F.; Maldague, X. Influence of different design parameters on a coplanar capacitive sensor performance. *NDT Int.* **2022**, *126*, 102588. [CrossRef]
23. Hilyard, N.C. *Mechanics of Cellular Plastics*; MacMillan: New York, USA, 1982; 360p.
24. Klempner, D.; Frisch, K.C. *Handbook of Polymeric Foams and Foam Technology*; Hanser Publishers: Munich, Germany, 1991; 413p.
25. Kirpļuks, M. Development of Renewable Feedstock Based Rigid Polyurethane Foam and Nanoclay Composites. Ph.D. Thesis, Riga Technical University, Riga, Latvia, 2020. Available online: https://ortus.rtu.lv/science/en/publications/31088 (accessed on 11 March 2024).
26. Beverte, I.; Shtrauss, V.; Kalpinsh, A.; Lomanovskis, U.; Cabulis, U.; Sevastyanova, I.; Gaidukovs, S. Dielectric Permittivity of Rigid Rapeseed Oil Polyol Polyurethane Biofoams and Petrochemical Foams at Low Frequencies. *J. Renew. Mater.* **2020**, *8*, 1151–1170. [CrossRef]
27. Beverte, I.; Gaidukovs, S.; Andersons, J.; Skruls, V. The Impact of Atmospheric Parameters on the Dielectric Permittivity Values of SikaBlock Block®-M150 and Other Rigid Polyurethane Foams Measured with a Capacitive One-Side Access Sensor. *Sensors* **2022**, *22*, 7859. [CrossRef] [PubMed]
28. *ISO 845:2006*; Cellular Plastics and Rubbers—Determination of Apparent Density. ISO: Geneve, Switzerland, 2006.
29. Beverte, I. Determination of Highly Porous Plastic Foams' Structural Characteristics by Processing LM Images Data. *J. Appl. Polym. Sci.* **2014**, *131*, N39477. [CrossRef]

30. Beverte, I.; Cabulis, U.; Andersons, J.; Kirpluks, M.; Skruls, V.; Cabulis, P. Anisotropy and Mechanical Properties of Nanoclay Filled, Medium Density Rigid Polyurethane Foams Produced in a Sealed Mold, from Renewable Resources. *Polymers* **2023**, *15*, 2582. [CrossRef]
31. Evaluation of Measurement Data—Guide to the Expression of Uncertainty in Measurement. JCGM 100:2008 GUM 1995 with Minor Corrections, 120p. Available online: https://www.bipm.org/utils/common/documents/jcgm/JCGM_100_2008_E.pdf (accessed on 18 March 2024).
32. International Vocabulary of Metrology—Basic and General Concepts and Associated Terms (VIM), 3rd Edition 2008 Version with Minor Corrections. JCGM 200:2012. Available online: https://www.bipm.org/utils/common/documents/jcgm/JCGM_200_2012.pdf (accessed on 18 March 2024).

Disclaimer/Publisher's Note: The statements, opinions and data contained in all publications are solely those of the individual author(s) and contributor(s) and not of MDPI and/or the editor(s). MDPI and/or the editor(s) disclaim responsibility for any injury to people or property resulting from any ideas, methods, instructions or products referred to in the content.